Flow dynamics control the effect of sphingosine-1-phosphate on endothelial permeability in

a microfluidic vessel bifurcation model

Griffin B. Spychalski
Department of Biomedical Engineering
The Ohio State University
Spring 2018

Thesis Committee:
Dr. Jonathan W. Song, Department of Mechanical & Aerospace Engineering, Comprehensive
Cancer Center, Faculty Advisor
Dr. Shaurya Prakash, Department of Mechanical & Aerospace Engineering

Abstract

Blood vessels are lined by endothelial cells that form a semipermeable barrier to restrict fluid flow across the vessel wall. The endothelial barrier is known to respond to various molecular mechanisms, but the effects of mechanical signals that arise due to blood flow remain poorly understood. Here, we report a microfluidic model that mimics the flow conditions and endothelial/extracellular matrix (ECM) architecture of a vessel bifurcation to enable systematic investigation of how flow dynamics that arise within bifurcating vessels guides the endothelial response to biochemical signals. Applying the strengths of our system, we further investigate the endothelial response to sphingosine-1-phosphate, a bioactive lipid that has demonstrated flow-dependent regulation of vascular permeability. We demonstrate that bifurcated fluid flow (BFF) that arises at the base of vessel bifurcations and laminar shear stress (LSS) that arises along downstream vessel walls induce a decrease in endothelial permeability. Furthermore, we identify that flow-dynamics and chaperone proteins regulate the endothelial response to S1P. Through pharmacological inhibition of S1P receptors 1 and 2, we report ligand-independent mechanical activation of S1P receptors 1 and 2, providing support for the role of G protein-coupled receptors as mechanosensors. These findings introduce BFF as an important regulator of vascular permeability, and establish flow dynamics as a determinant of the endothelial response to S1P.

Acknowledgements

I would like to thank my research advisor, Dr. Jonathan Song, for his encouragement, motivation, and support throughout my time as a member of his lab. Dr. Song has been a tremendous role model for the past two and a half years, encouraging me to pursue my greatest ambitions. He is a central factor in my decision to work towards an MD-PhD in the next stage of my training, and I am sincerely thankful for the role that he has played in my path towards a career in scientific research.

Additionally, I would like to thank Ehsan Akbari for his mentoring and support from my earliest days in the Song Lab. As a partner on this project, Ehsan was instrumental in completing these experiments. Always a reliable resource for advice or knowledge, Ehsan served as an inspiration as I shaped my role in Dr. Song's lab. Furthermore, I would like to acknowledge Kaushik K. Rangharajan and Dr. Shaurya Prakash for their valuable contributions to our research collaborations, and thought-provoking discussions. Finally, I would like to thank all the past and present members of the Microsystems for Mechanobiology and Medicine Lab for their support and enthusiasm for undergraduate research.

I acknowledge The Ohio State University College of Engineering for the opportunity and funding to conduct my honors thesis research. I also acknowledge funding from the Undergraduate Summer Research Program of The American Heart Association Great Rivers Affiliate and a Barry M. Goldwater Scholarship. This work was supported by the Pelotonia Fellowship Program.

Table of Contents

List of Figures

1. BACKGROUND AND MOTIVATION

Blood vessels comprise a hierarchical network that transports oxygen and nutrients throughout the body.[1] The endothelial cells that line the inner wall of blood vessels form a semipermeable barrier to regulate fluid and solute transport between blood and surrounding tissue.[2] Transendothelial flow, which occurs as fluid and solutes pass in the paracellular space between adjacent endothelial cells (ECs),[3,4] is regulated by exogenous growth factors and cytokines like vascular endothelial growth factor (VEGF), and endothelium-derived factors like nitric oxide (NO).[4] Endothelial barrier dysfunction is characteristic of inflammation[5] and atherosclerosis,[6] and increased endothelial permeability is often concomitant with pathological angiogenesis, the excessive formation of new and immature blood vessels with poor blood perfusion (Fig. 1).[7]

1.1. Sphingosine-1-phosphate as a determinant of vascular development

Sphingosine-1-phosphate (S1P) is an extracellular bioactive lipid synthesized primarily within endothelial cells and erythrocytes,[8,9] and is enriched within the intraluminal space.[10] S1P
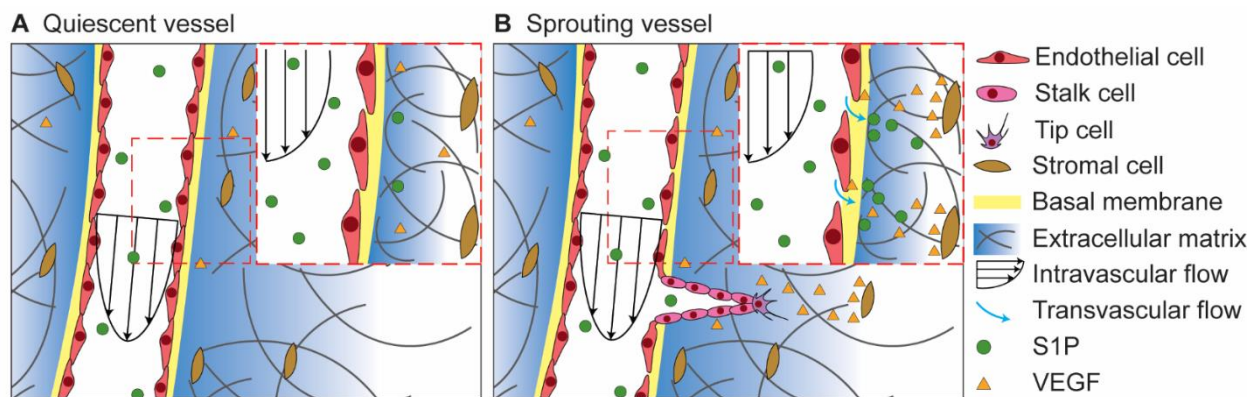
Figure 1: Physiochemical microenvironment of angiogenesis. (A) Intact blood vessel adhered to the extracellular matrix. Endothelial cells are anchored to the basement membrane, which resists intraluminal shear stress. *Inset:* Tight endothelial junctions limit transvascular flow, and decrease vascular permeability. (B) Biochemical gradient of stromal-secreted VEGF induces angiogenesis. Extension of tip cell-led vessel sprouts is supported by increased proliferation and elongation of stalk cells during lumen formation. *Inset:* Local VEGF gradient loosens nearby endothelial cell junctions, resulting in elevated transvascular flow and increased vascular permeability. Blood-borne solutes (e.g. S1P) leaks into the interstitial space. Adapted from Akbari, Spychalski, and Song.[11]

demonstrates a steep concentration gradient from the blood circulation to extravascular microenvironment,[8] which is believed to guide vascular development and maintenance, in addition to immune cell trafficking.[10] The S1P gradient is maintained by a combination of enzymatic degradation within tissues and S1P association with chaperone proteins in blood circulation. Within tissues, parenchymal cells produce S1P lyase that enzymatically depletes extravascular S1P.[12] In the circulation, S1P binds to plasma protein chaperones, namely albumin and high-density lipoprotein (HDL), which drives an increase in the concentration of circulatory S1P and influences how S1P interacts with cell receptors.[13]

S1P is implicated in controlling various mechanisms of vascular development, including sprouting angiogenesis,[14,15] perivascular recruitment,[16] vascular tone,[17] and endothelial barrier function.[14,18,19] S1P elicits such responses by signaling through G protein-coupled receptors; five receptors for S1P have been identified, named $S1P_{1-5}$ (Fig. 2).[20] $S1P_1$ and $S1P_3$ are the primary S1P
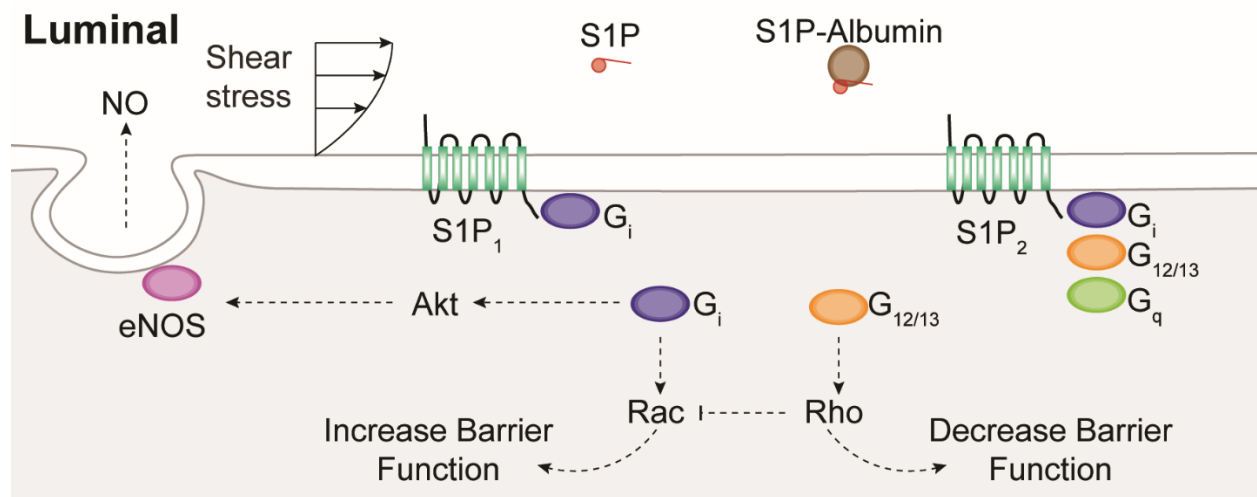
Figure 2. **Sphingosine-1-phosphate (S1P) signals through competing receptors.** Spingosine-1-phosphate is a bioactive lipid that acts through a group of five identified G protein-coupled receptors, $S1P_{1-5}$. While $S1P_1$ couples exclusively with Gαi/o, $S1P_2$ couples with Gαi/o, Gα12/13, and Gαq. Activation of Gαi/o acts through the Rac pathway to increase endothelial barrier function, while activation of Gα12/13 activates the Rho pathway to inhibit Rac activity and decrease endothelial barrier function. Flow dynamics – namely shear stress – have been shown to influence S1P signaling by increasing expression of $S1P_1$. Association with plasma chaperone proteins, including albumin, contributes to the intraluminal compartmentalization of S1P and can enhance S1P and S1P receptor binding.
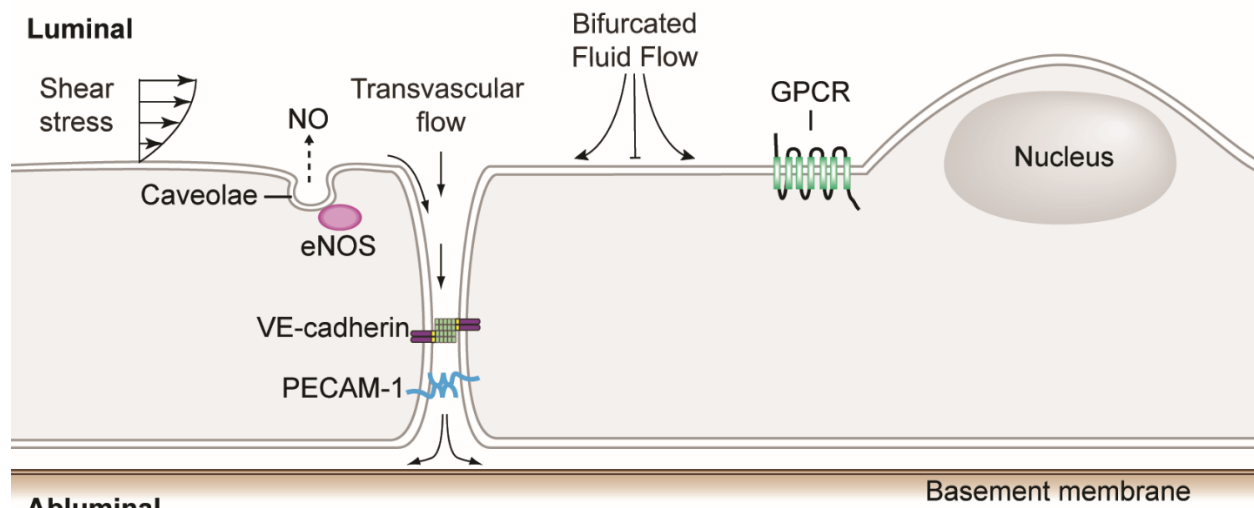
Figure 3. Endothelial mechanosensors. Intraluminal shear stress due to blood flow and transvascular flow that occurs as plasma extravasates have been identified as determinants of angiogenesis, vascular permeability, and vessel tone. Shear stress is known to activate endothelial nitric oxide synthase (eNOS) production of nitric oxide, a determinant of vascular development. G protein-coupled receptors (GPCR) are also believed to be mechanosensitive, with previous reports of ligand-independent mechanical activation. In contrast to shear stress and transvascular flow, the effects of bifurcated fluid flow that arises due to impinging flow at the base of vessel bifurcations remains poorly understood.

receptors expressed on ECs,[21] but S1P$_2$ can be found on larger vessels, lung microvasculature, and tumor and inflamed vasculature.[22] While S1P$_1$ exclusively couples with Gαi/o proteins, S1P$_2$ and S1P$_3$ couple with Gαi/o, Gαq, and Gα12/13[10] (Fig. 3). Gαi/o activation increases endothelial barrier function by signaling through the Rac pathway;[10] Gαi/o also signals through Akt to activate endothelial nitric oxide synthase (eNOS) to stimulate NO production.[23] In contrast, Gα12/13 activation decreases endothelial barrier function by signaling through the Rho pathway, inhibiting Rac signaling.[10] Therefore, it follows that S1P$_1$ maintains barrier integrity, while S1P$_2$ disrupts endothelial barrier function during vascular pathologies. However, the role of S1P$_2$ is less definitive, as it has been found to demonstrate tissue-specific responses depending on the experimental context; for example, within tumor vasculature, S1P$_2$ is found to be a negative regulator of sprouting angiogenesis and decreases endothelial permeability.[22]

3

1.2. Blood flow-dependent regulation of S1P and S1P receptors

S1P receptor activity and expression is enhanced by fluid mechanical forces, such as shear stress due to blood flow. Shear stress has been shown to increase expression of S1P$_1$,[14,24,25] and blood flow also downregulates S1P lyase transcription.[12] Shear stress has been demonstrated to enhance S1P$_1$ signaling, and is even hypothesized to mechanically activate S1P$_1$ independent of ligand binding.[10,14] Fluid forces like shear stress can regulate vascular permeability through endothelial mechanosensors, including the endothelial glycocalyx[26], integrins[27], and G protein coupled receptors[28] like S1P$_1$ (Fig. 2). Moreover, shear stress has been identified as a determinant of sprouting angiogenesis both *in vivo*[14,29,30] and *in vitro* (Fig. 3).[31–33] Taken together, these studies establish a role for flow dynamics in regulating vascular function and demonstrate the importance of vascular disease model systems that permit the co-application of precisely characterized mechanical and chemical signals.

1.3. Quantitative Analysis of Endothelial Permeability

Vascular permeability is typically quantified *in vivo* using intravital microscopy to monitor the extravasation rate of a fluorescently labeled molecular tracer after intravenous injection.[34,35] Yet *in vivo* assays often cannot specify precisely controlled physiochemical conditions to isolate the mechanistic determinants of vascular barrier function. *In vitro* microvascular models present functional and potentially high-throughput tools that enable the facile measurements of endothelial permeability under controlled biophysical and biochemical stimuli.[36–39] In this context, microfluidic techniques provide rapidly prototyped platforms to study endothelial barrier function while replicating the hemodynamic conditions, the three dimensional (3D) endothelial-extracellular matrix (ECM) interface topology, and the length scales of an intact blood

vessel.[39,11,40–42] However, previously described microfluidic models were often limited to straight microchannels embedded within or laterally adjacent to semi-porous ECM. The straight channel geometry fails to reconstitute the local flow dynamics of branching microvascular networks, which can omit significant governing parameters of vascular function (Fig. 3).[5,11,43] Consequently, the endothelial permeability outcomes that arise due to the local flow dynamics produced by branching vessel geometry remain poorly understood.

To address the limitations of existing *in vitro* systems, we developed a 3D microfluidic model of bifurcating vessel structures that enables measurement of the local endothelial permeability in response to the flow dynamics at the bifurcation point (BP) and the branched vessel (BV) regions (Fig. 2).[42] The endothelial permeability data were reported as the endothelial hydraulic conductivity using the permeability coefficient L_P. Moreover, we investigated the role of flow dynamics in regulating the endothelial response to S1P, and we applied pharmacological inhibitors of S1P receptors $S1P_1$ and $S1P_2$ to investigate how flow dynamics act through S1P's G protein-coupled receptors to co-regulate endothelial permeability.

Here, we show that both bifurcated fluid flow (BFF) (~38 dyn/cm^2 stagnation pressure and approximately zero shear stress) specified at the BP and laminar shear stress (LSS) (3 dyn/cm^2) in the BV regions result in an initial increase in endothelial permeability over the first hour, followed by a significant decrease in permeability after 6 hours. In addition, we demonstrate that S1P induces increased L_P under static conditions, which was negated when applied with flow dynamics or albumin chaperones. Finally, we report the ligand-independent mechanical activation of $S1P_1$ and $S1P_2$. Taken together, these results reveal how fluid forces regulate the response in endothelial permeability to S1P and provide insights into how association with chaperone proteins influences S1P signaling.

Our conclusions regarding the stabilizing effect of BFF on endothelial permeability provide novel insights into how branching vascular geometries regulate vascular development through flow dynamics. Furthermore, we demonstrate the utility of our system to spatially apply gradients of physiologically compartmentalized signaling molecules. Such advances in state-of-the-art biomimetic modeling of the vasculature can enable significant progress in our understanding of how the physiochemical determinants of vascular barrier function regulate vascular development, which can inform potential therapeutic insights on addressing pathological vascular permeability.

2. METHODOLOGY

2.1. Design and characterization of microfluidic vessel bifurcation model

A 3D *in vitro* microfluidic model of a branching vessel structure was designed, fabricated, and characterized to elucidate the effects of flow dynamics on endothelial permeability (Fig. 2).[42] The polydimethylsiloxane (PDMS) microfluidic device enables: (i) formation of an EC monolayer on a 3D ECM scaffold, (ii) replication of the physiological hemodynamic conditions of vessel bifurcations, including impinging bifurcated fluid flow (BFF) that stagnates at the vessel bifurcation and intravascular laminar shear stress (LSS) in the downstream daughter vessel analogues, (iii) systematic application of transvascular flow (TVF) by controlling the difference between the intravascular pressure (IVP) and the interstitial fluid pressure (IFP) in the microfluidic device, and (iv) measurement of the endothelial hydraulic conductivity under the effects of local fluid forces imparted on the endothelium.

The PDMS microfluidic device features microchannels that are 50 μm in height. The bifurcating vessel geometry is produced by a single parent microchannel (1300 μm in width) lined with ECs that branches into two daughter branched vessel analogues (both 500 μm in width)

separated by a central ECM channel (400 µm in width) containing polymerized type I collagen (3 mg/mL concentration) (Fig. 4B-D). The central ECM channel was filled with a collagen hydrogel using capillary filling. Importantly, the semi-porous 3D scaffold abluminal to the endothelial layer can be remodeled, which is necessary to assess vascular permeability and angiogenic sprouting.[44] At the branching location, two PDMS microposts with 100 µm wide apertures or gaps (Fig. 4) were fabricated to confine the ECM gel within the designed compartment while allowing for direct contact between the human umbilical vascular endothelial cells (HUVECs) and the adjacent 3D ECM (Fig. 4E, F). HUVECs were selected for these studies because vessel leakage induced by
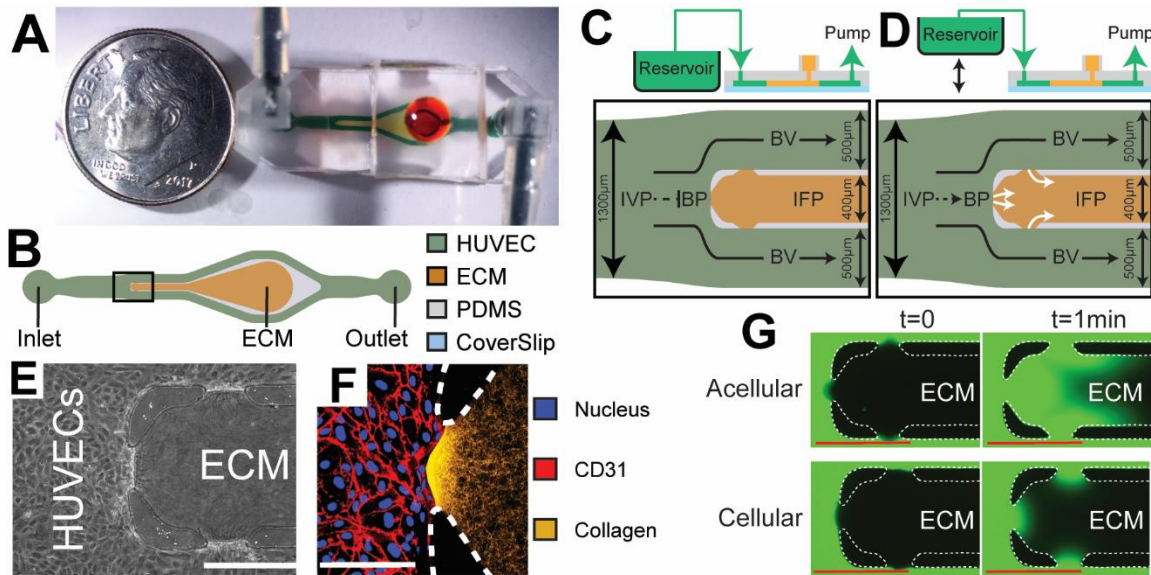
Figure 4. Microfluidic bifurcating vessel model for endothelial hydraulic conductivity measurements. (A) The photograph of the device stained with green dye in the perfusion channels and orange dye in the extracellular matrix (ECM) compartment. (B) Schematic of the microfluidic platform depicting the microchannels seeded with human umbilical vascular endothelial cells (HUVECs, green) branching around the central ECM (orange) compartment. (C) Magnified view of the bifurcation region (black box in A) depicting the apertures at the bifurcation point (BP) and branched vessel (BV). (D) Elevating the reservoir hydrostatic pressure produces a controlled pressure difference between the intravascular pressure (IVP) and interstitial fluid pressure (IFP), inducing transvascular flow (TVF) from both the BP and BV (white arrows). (E) Representative phase contrast image of the bifurcation region fully seeded with HUVECs adjacent to the polymerized ECM matrix. Scale bar is 500 µm. (F) Representative confocal reflectance image of the aperture at BP depicting the confluent HUVEC monolayer with well-defined junctions adjacent to the supporting fibrous ECM. The white dotted lines depict the PDMS microposts. Scale bar is 100 µm. (G) Representative fluorescence images of acellular versus cellular (or HUVEC-lined) microchannels with FITC conjugated dextran (10 kDa). Under a similar inlet pressure, the HUVEC monolayer at each of the apertures uniformly suppresses the level of transendothelial fluid flow, thereby confirming effective HUVEC barrier function. Scale bars are 500 µm.

physiological stimuli is known to preferentially occur in postcapillary veins.[7] In addition, HUVECs are known to elicit responses to shear stress, including steady production of NO.[45] The microchannels were lined with HUVECs (Fig. 4E) that formed a confluent monolayer with defined adherent junctions (Fig. 4F); effective barrier function provided by the HUVEC monolayer was confirmed at each of the HUVEC-ECM apertures. (Fig. 4G).

Our microfluidic bifurcating vessel model enables simultaneous application of LSS with TVF in the BV regions, which is an attribute it shares with previously described parallel vessel models.[32] However, our bifurcating vessel model uniquely allows co-application of TVF with BFF at the BP. In addition, our microfluidic model has the capability for independent control of TVF levels from the perfusion rate. This capability was achieved through precise control of the transendothelial pressure difference or the difference in hydrostatic pressures in the luminal (IVP) and interstitial domains (IFP) (Fig. 4C, D) while perfusing the microchannels at a fixed flow rate, maintaining constant BFF and LSS with varying TVF. Therefore, our bifurcation model enables decoupling of the effects of TVF on endothelial permeability from the effects of BFF and LSS. Shear stress levels in postcapillary veins are typically within 1-4 dyn/cm^2.[43] Based on our numerical modeling results, perfusing the microfluidic devices at 10 µL/min flow rate produces 3 dyn/cm^2 LSS oriented tangential to the endothelium in the BV regions that is within the range of physiological venous shear stress levels (Fig. 6A). Furthermore, this flow rate generated BFF with a stagnation pressure of 38 dyn/cm^2 and approximately zero shear stress at the BP (henceforth referred to as 38 dyn/cm^2 BFF) (Fig. 6A). Two different levels of TVF were tested by controlling the reservoir elevation: average zero TVF when IVP≈IFP and ~1 µm/s under IVP - IFP = 1.5 cm H_2O (Figs. 6A). Furthermore, particle tracking velocimetry was used to validate the numerically predicted flow dynamics in the microchannels.

2.2. Endothelial hydraulic conductivity (L_P) measurements

To study endothelial permeability, we quantified endothelial hydraulic conductivity as the permeability coefficient, L_P. The Starling hypothesis is often employed to characterize the transendothelial exchange of plasma[46] [Eq. 1]:

$$J_V = L_P(\Delta P - \sigma \Delta \pi) \quad (1)$$

where ΔP is the hydrostatic pressure difference across the endothelial monolayer, $\Delta \pi$ is the solute oncotic pressure difference across the endothelium, σ is the reflection coefficient, J_V is the volumetric flux across the vessel wall, and L_P is the endothelial hydraulic conductivity. The oncotic effects are negligible in *in vitro* models of microvasculature due to the homogenous media composition.[47] Therefore, the hydrostatic pressure difference across the endothelial monolayer is the main driving force inducing transvascular flow across the endothelial monolayer at each aperture. Thus, L_P could be measured by estimating ΔP at each aperture, along with quantification of volumetric flux levels of fluorescent tracer dye.

Accurate L_P measurements require estimation of the level of the hydrostatic pressure directly below or abluminal to the endothelial monolayer. The abluminal hydrostatic pressure was estimated by calculating the equivalent hydraulic resistance of the ECM using a computational model of the microfluidic platform. To perform this computational modeling, the bulk hydraulic permeability of the 3 mg/mL collagen type I matrix was experimentally measured using a simple straight flow channel as previously described.[48] The measured value for the collagen bulk hydraulic permeability ($0.34 \pm 0.2 \ \mu m^2$) was within the range of the previously reported measurements.[49] The measured bulk hydraulic permeability was then used as an input for the computational model to estimate the equivalent hydraulic resistance of the ECM.
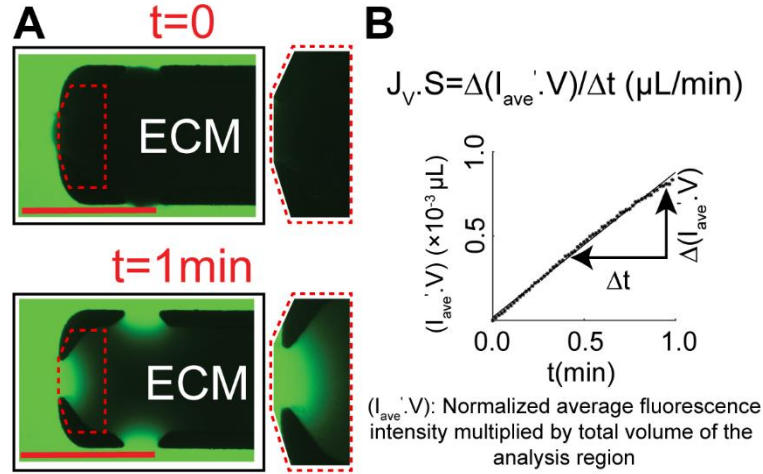
Figure 5. **Quantification of transendothelial volumetric flux (J_V).** (A) The representative epifluorescence images of the cellular microfluidic platform perfused with 10μM FITC- Dextran. A user-defined region of interest was used to analyze the rate of convective transport for the FITC-Dextran across the endothelial monolayer at each aperture (dashed red line). Scale bars, 500 µm. (B) The rate of increase in normalized average fluorescence intensity within the defined Eulerian control volume multiplied by the volume of the analysis region ($I'_{ave}.V$) equates the level of transendothelial flux (J_V) multiplied by the monolayer area (S). The R^2 value of the linear fit was 0.98.

Next, the transendothelial flux was measured following each experimental test condition by monitoring the extravasation rate of FITC conjugated 10 kDa dextran (10 µM) as a fluorescently tagged solute under 1.5 cm H_2O pressure difference between IVP and IFP (IVP = 1.5 cm H_2O and IFP=0). The net transport of the fluorescent solute was quantified by using the principle of conservation of mass within an Eulerian control volume (Fig. 5, red dotted box). The level of abluminal pressure was then calculated using the ECM hydraulic resistances and the quantified level of transendothelial volumetric flux across the endothelium at each aperture. Subsequently, the values for abluminal pressure were used to estimate the level of transendothelial pressure difference across each aperture.

From the quantified values of ΔP and J_V, L_P could be calculated from the Starling hypothesis [Eq. 1]. The L_P measurement method is completely detailed by Akbari et al[42].

10

2.3. Chemical Reagents

Stock solution of chaperone-free sphingosine-1-phosphate (S1P) was prepared by dissolving S1P (Cayman Chemical) in 1x Dulbecco's phosphate-buffered saline (DPBS) (Corning) with 0.3N NaOH (Sigma-Aldrich) to achieve stock concentration of 10 mM. To prepare S1P associated with chaperone proteins, S1P (Avanti Polar Lipids) was suspended in methanol:water (95:5) and heated to 65 °C and sonicated to produce a 0.5 mg mL^{-1} S1P solution. The solution was dried under dry nitrogen steam and dissolved in 1x DPBS with 4 mg mL^{-1} fatty-acid free bovine serum albumin (BSA) (Sigma) to produce stock solution of 125 µM. Stock solution of W123 (Cayman) was prepared by dissolving in DMSO to stock concentration of 50 mM. Stock solution of JTE-013 (Cayman Chemical) was prepared by dissolving in DMSO to stock concentration of 10 mM.

2.4. Fabrication of the microfluidic platform

The microfluidic platform was fabricated using polydimethylsiloxane (PDMS) with soft lithography to pattern and generate designed PDMS structures. The platform outline was designed using AutoCad (AutoDesk) and printed on transparency masks (CadArt). The 50 µm tall monolithic microchannel features were patterned on an N-type 4 in silicon wafer (University Wafers) using SU-8 2050 (MicroChem) and exposed with ultraviolet (UV) radiation to yield the molds used to cast PDMS. Silicon elastomer base and curing agent (Ellsworth Adhesives) were mixed at a ratio of 10:1, degassed and cured in an oven overnight at 65 °C on the Si master to form the patterns in PDMS. The cured PDMS was peeled from the silicon master and cut into individual devices. To access the microchannels for perfusion and extracellular matrix (ECM) injection, ports were created with 1.5 mm biopsy punches (Militex) prior to sealing the channels with glass coverslips. Individual devices were irreversibly bonded against a glass coverslip using plasma

treatment. The microfluidic devices were baked overnight at 65 °C and UV sterilized for 30 min prior to experimental usage.

2.5. Type I collagen hydrogel preparation

A type I collagen-based hydrogel solution was used to construct a 3D extracellular matrix (ECM) mimic in the microchannel. Rat tail collagen type I (Corning) was mixed with 10x Dulbecco's phosphate-buffered saline (DPBS) (Corning), 1 N NaOH (Sigma-Aldrich), double distilled sterile water, and human fibronectin (Fisher Scientific) to yield an ECM solution with final concentrations of 3 mg mL^{-1} collagen with a pH of 7.4, 10 µg mL^{-1} fibronectin, and 1x DPBS. This ECM solution was injected into the collagen compartment and incubated for 24 hours in an incubator at 37 °C to form a fully-polymerized 3D ECM.

2.6. Preparation of HUVECs

Human umbilical vein endothelial cells (HUVECs) were commercially purchased (Lonza) and maintained using endothelial growth media (EGM) (Lonza) at 37 °C with 5% CO_2. HUVECs with passage numbers of 6-12 were washed with 1x DPBS without Mg or Ca (Corning), followed by cell removal using 0.05% Trypsin-EDTA (Thermo Fisher) for 45 seconds to detach the ECs from the cell culture flask. The detached cells were re-suspended in fresh EGM and prepared for the experiments.

2.7. Microfluidic cell culture of HUVECs

To prepare the inner walls of the microfluidic devices to facilitate endothelial cell adhesion, devices with polymerized collagen gel were flushed with 10 µg mL^{-1} human fibronectin solution

diluted in 1x DPBS and incubated for 2 hours at 37 °C. Fibronectin-coated microfluidic channels were then flushed with EGM and incubated overnight at 37 °C prior to seeding the endothelial cells into the perfusion channels. HUVECs were removed from the cell culture flask with trypsin and re-suspended in EGM at 40 000 cells per µL. The microfluidic channels were injected with the cell suspension and incubated overnight at 37 °C, with EGM droplets applied after 1 hour of incubation 37 °C. HUVECs were grown to confluence (24 hours after initial seeding) to cover the inner surfaces of the perfusion microchannels.

2.8. Microfluidic perfusion assay

Translucent tubing with 0.8 mm inner diameter (Cole-Palmer) connected with barbed elbow and T-connectors (Cole-Palmer) were used to perfuse the microfluidic platform. The assembled tubing circuits were autoclaved using hot steam sterilization and connected to the inlet and outlet ports on the microfluidic devices seeded with HUVECs. The inlet port was connected to an EGM reservoir and the outlet port was connected to a 10 mL BD-syringe (Fisher Scientific) mounted on a syringe pump (Harvard Apparatus) to continuously withdraw EGM from the inlet reservoir. The intravascular pressure in the perfusion microchannels was adjusted via the hydrostatic pressure head of the media reservoir to enable independent control of TVF from BFF and LSS.

2.9. Pharmacological antagonization of S1P receptors

S1P1 was pharmacologically degraded using competitive antagonist W123, which binds to S1P1 to initiate ligand-induced internalization. HUVEC-seeded microdevices were flushed with EGM, followed by incubation with EGM supplemented with 10 µM W123 for 3 hours at 37 °C. Before application of experimental test conditions, the devices were flushed with EGM to remove W123.

S1P2 was pharmacologically degraded using selective antagonist JTE-013. HUVEC-seeded microdevices were flushed with EGM, followed by incubation with EGM supplemented with 200 nM JTE-013 for 30 min at 37 °C. The devices were flushed with EGM to remove JTE-013 prior to application of experimental test conditions.

2.10. Immunofluorescence

Following each experimental test condition, microfluidic devices were flushed three times with 1x DPBS and incubated with 3% paraformaldehyde (Sigma-Aldrich) in 1x DPBS for 30 min. The microfluidic devices were flushed three times with 1x DPBS and incubated with blocking bluffer, which consists of 5% bovine serum albumin (BSA) (Sigma-Aldrich) and 0.1% Triton X-100 (Sigma-Aldrich) for 1 hour. Next, the devices were rinsed three times with 1x DPBS and incubated for 90 min with mouse anti-human CD31 primary antibody (Agilent Technologies) diluted by 1:20 in 1x DPBS with 1% BSA. The devices were flushed three times with 1x DPBS and incubated for Alexa 555-labeled goat anti-mouse secondary antibodies (Thermo Fisher) diluted by 1:500 in 1x DPBS with 1% BSA. Microchannels were flushed three times with 1x DPBS and allowed to incubate at 4 °C with gravity-driven flow to remove excess antibody. The microfluidic devices were incubated with DAPI (Sigma-Aldrich) diluted by 1:1000 in double distilled water for 3 min to stain for HUVEC nuclei. The devices were finally flushed three times with 1x DPBS before imaging.

2.11. Image acquisition

The devices were imaged using phase contrast (TS-100, Nikon) with a 10x air objective prior to starting treatment to examine the quality of endothelial seeding. After treatment under each

condition, the HUVECs were imaged using phase contrast followed by fluorescence imaging using epifluorescence microscopy (473 nm excitation/488 nm emission, TS-100, Nikon) with a 10x air objective to monitor the transendothelial transport of 10µM FITC conjugated 10 kDa dextran suspended in EGM (Sigma). The fluorescence imaging was performed at 1 s intervals to capture the dynamic transendothelial transport of fluorescent tracer. Confocal microscopy was performed on the stained microdevices using a laser scanning confocal scope (A1R, Nikon) with a 40x oil immersion objective. A laser type light source was used to excite DAPI (blue) and Alexa 555-conjugated goat secondary antibody stained CD31 (red). Furthermore, confocal reflectance microscopy was used to visualize the 3D structure of the collagen matrix.

2.12. Measurement of ECM bulk hydraulic permeability

The permeability characterization of bulk collagen gel was achieved using a simple straight flow channel (5 x 0.5 x 1 mm) as previously reported.[48] The 3 mg mL^{-1} collagen gel solution was prepared as previously described and injected in the straight microchannel followed by polymerization overnight at 37 °C. A 10 µM solution of 10 kDa FITC-dextran (Sigma) was prepared in 1x DPBS (Corning) and perfused through the 3D type I collagen-based ECM by applying a controlled level of hydrostatic pressure (~240 Pa) along the channel. The hydrostatic pressure head was generated by inserting a pipette tip in the inlet port filled with 10 µM FITC-dextran solution. The moving FITC-dextran dye interface was monitored over time using epifluorescence time lapse imaging as described. An in-house developed MATLAB code was used to quantify the total increase in fluorescent signal within a user-defined Eulerian control volume to estimate the level of influx. Average hydraulic permeability of the ECM matrix was reported based on Darcy flow assumption.

2.13. Quantification of transvascular flow

A custom MATLAB code was used to analyze the epifluorescence timelapse images of the transendothelial transport of 10 kDa FITC-dextran. Transendothelial flux was quantified based on conservation of mass equation for a user-defined Eulerian control volume sharing an overlapping boundary with the endothelial monolayer (Fig. 5). For each measurement, the user-defined control volume was adjusted so that the endothelial monolayer overlapped with the control volume boundary. The total increase in fluorescent signal within the control volume was quantified over time to estimate the transendothelial flowrate. The monolayer area was estimated by fitting a polygon on the ECM interface at each aperture.

2.14. 3D computational model

Numerical analysis was performed by Ehsan Akbari and Kaushik K. Rangharajan using COMSOL Multiphysics (v.5.2). The device geometry was imported from AutoCAD (actual experimental design) and extruded to a height of 50 µm matching the height of the device. Governing equations were solved under steady-state, isothermal, incompressible, and laminar flow conditions. Continuity equations were solved for the entire geometry with the Navier-Stokes equations solved for the microchannels and the Brinkman equation solved inside the ECM to account for collagen permeability and porosity. No-slip boundary conditions were imposed on all PDMS walls. The device inlet was assigned a constant pressure according to the reservoir pressure head, as the media was perfused in to the device from the bottom of the reservoir (Fig. 4C and D). The outlet of the device was connected to the syringe pump in the experiments, and therefore in the numerical model, a constant velocity boundary condition matching the experimental flow rate was assigned to the outlet port. The collagen port was assigned a constant pressure according to the column of media

that was placed on top of the collagen port over the course of the experiments (Fig. 4C and D). Solutions from coarse meshes were re-iterated with finer meshes until mesh-insensitive solutions were achieved.

2.15. Statistical methods

Numerical values reported in results and discussion section represent the mean ± the standard error of the mean for at least three replicates for each experimental test condition. Two-sided student t-tests were used to report the statistical significance between each pair of experimental test conditions for L_p. Levels of significance were reported using the following: * indicates p-value < 0.05, ** indicates p-value < 0.01, and *** indicates p-value < 0.001.

3. RESULTS AND DISCUSSION

3.1. Bifurcated fluid flow (BFF) and laminar shear stress (LSS) decrease endothelial hydraulic conductivity

After characterizing the microfluidic model flow dynamics, we next monitored changes in L_P in response to BFF and LSS in the absence of TVF. HUVECs treated with 38 dyn/cm^2 BFF for 1 hour showed an initial 3.0-fold increase in L_P followed by a 71% decrease over 6 hours compared to the static control condition (Fig. 6B, C). Similarly, treatment with 3 dyn/cm^2 LSS for 1 hour showed an initial 1.8-fold increase in L_P followed by a 76% decrease over 6 hours compared to the static control condition (Fig. 6B, D). Our results suggest time-dependent regulation of HUVEC L_P in response to LSS matching the trends previously reported for HUVECs.[50,51] However, to our
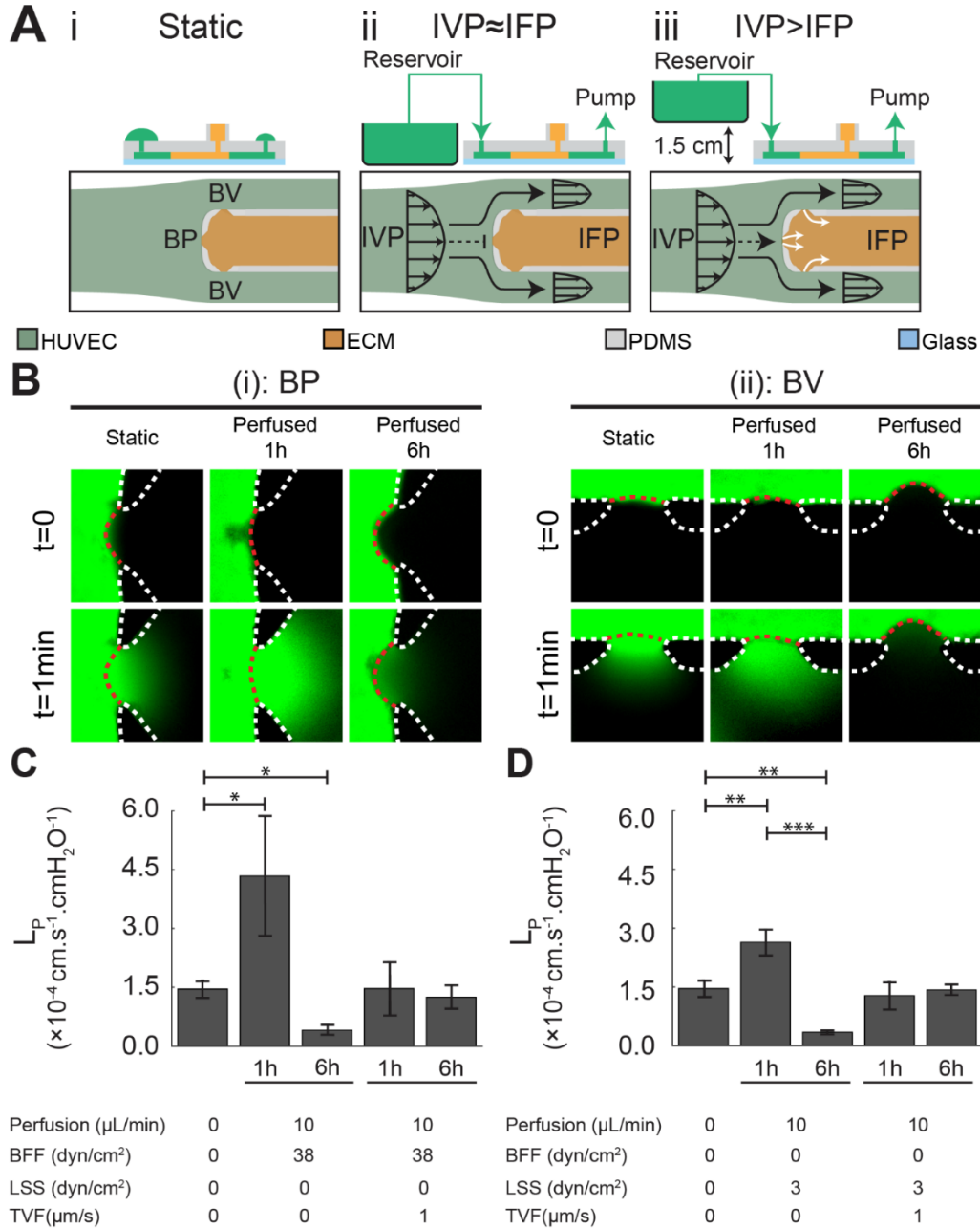
Figure 6. Bifurcating vessel flow dynamics transiently control endothelial permeability. (A) Schematic of the microfluidic platform, depicting the experimental outline of: (i) static control, (ii) perfused microfluidic device generating bifurcated fluid flow (BFF) (black dashed line) and laminar shear stress (LSS) (black solid lines) under equilibrated intravascular pressure (IVP) and interstitial fluid pressure (IFP), which results in minimal transvascular flow (TVF), and (iii) perfused microfluidic platform under elevated IVP, which results in luminal to abluminal TVF (white solid lines). (B) Representative images of L_P measurement after treatment with each experimental test condition at (i) BP and (ii) BV. The white dotted lines represent the PDMS microposts. The red dotted lines represent the semipermeable HUVEC monolayer at each aperture. Scale bars are 100 μm. (C) Quantitative effects of 38 dyn/cm^2 BFF and ~1 μm/s TVF on endothelial hydraulic conductivity after 1 hour and 6 hours of treatment, compared to static control condition. (D) Quantitative effects of 3 dyn/cm^2 LSS and ~1 μm/s TVF on endothelial hydraulic conductivity after 1 hour and 6 hours of treatment, compared to static control condition. *, $p < 0.05$. **, $p < 0.01$, ***, $p < 0.001$.

knowledge, this is the first report of the time-dependent regulation of HUVEC L_P in response to BFF.

Next, we monitored changes in L_P in response to co-application of TVF with BFF and LSS. Co-application of ~1 µm/s average TVF with BFF and LSS at BP and BV respectively, elicited a competing effect by rescuing the hydraulic conductivity of the HUVEC monolayer to the static control condition level after 1 hour and 6 hours of perfusion (Fig. 6C, D). Therefore, these findings suggest that the effect of TVF on endothelial permeability counteracts against the stabilization outcomes of BFF and LSS.

3.2. Flow dynamics and albumin chaperones suppress sphingosine-1-phosphate (S1P)-induced increases in endothelial hydraulic conductivity

We next studied how co-application of S1P with flow dynamics alters the endothelial response in L_P. HUVECs treated with 500 nM S1P under static conditions for 6 hours showed a 7.9-fold increase in L_P compared to the static control condition (Fig. 7B). Conversely, treatment with 500 nM S1P and 3 dyn/cm^2 LSS for 6 hours did not demonstrate a statistically significant increase compared to the 3 dyn/cm^2 LSS control (Fig. 7B). Treatment with 500 nM S1P and 38 dyn/cm^2 BFF for 6 hours demonstrated a modest increase in L_P compared to BFF and LSS control conditions at BP and BV respectively (Fig. 6B). These results indicate that the static increase in endothelial permeability after treatment with S1P is negated by fluid forces from BFF and LSS.

After investigating how fluid forces influence the endothelial response to S1P, we investigated chaperone-dependent responses in L_P by applying S1P associated with chaperone protein bovine serum albumin (S1P-BSA). Application of 500 nM S1P-BSA under static conditions over 6 hours did not show a significant increase in L_P compared to static control

conditions (Fig. 7B). Furthermore, application of 500 nM S1P-BSA and exposure to BFF and LSS over 6 hours at BP and BV respectively, did not show a significant increase in L_P compared to
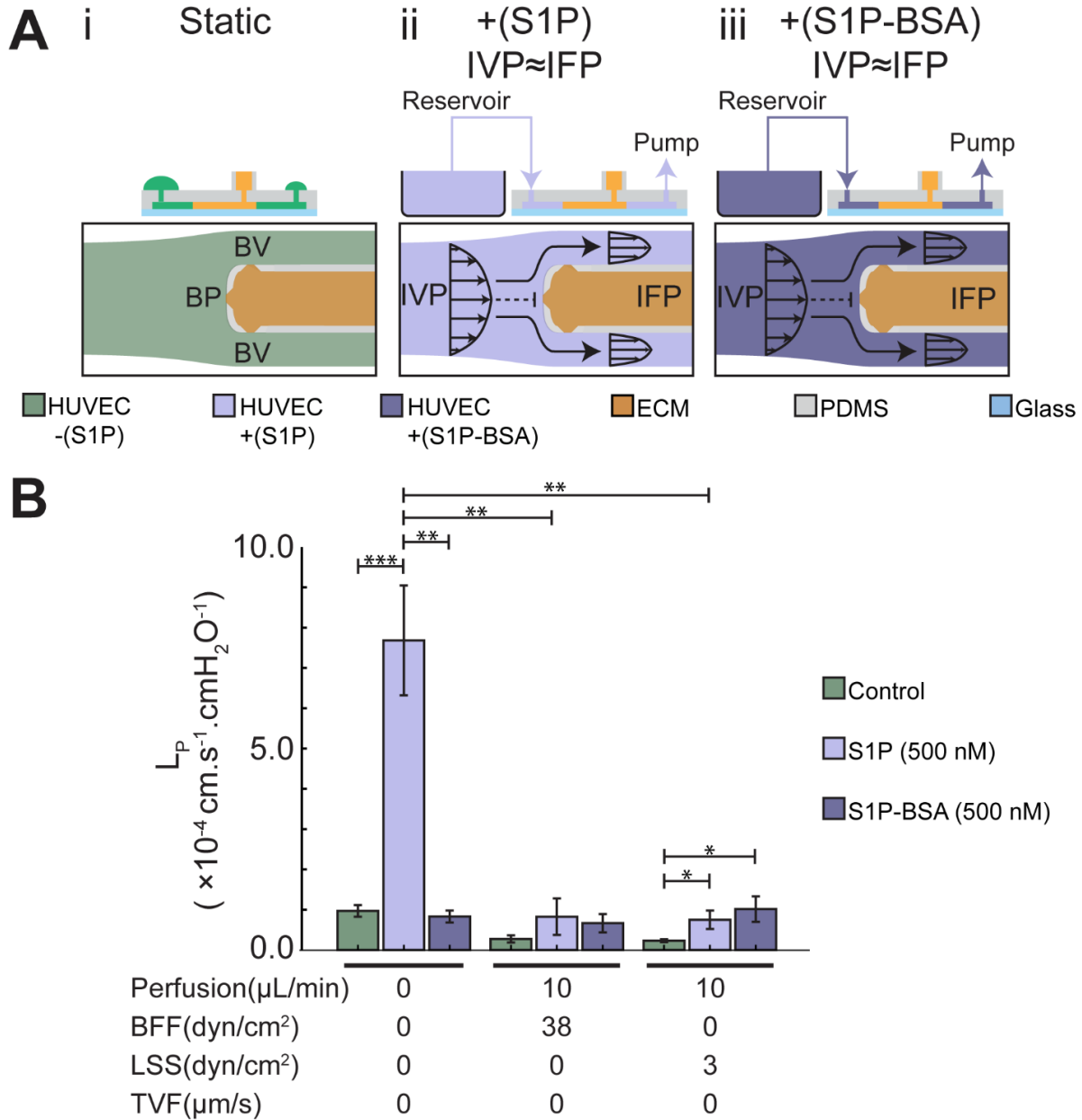
Figure 7. Endothelial permeability response to sphingosine-1-phosphate depends on flow dynamics and albumin chaperones. (A) Schematics of the experimental conditions: (i) static control, (ii) perfused microdevice in the absence of transvascular flow and addition of sphingosine-1-phosphate (S1P) (500 nM) to perfusion media, and (iii) perfused microdevice in the absence of TVF and addition of S1P associated with bovine serum albumin (S1P-BSA) (500 nM) to the perfusion media. (B) Quantitative effects of application of S1P increases L_P under static conditions, but co-application BFF and LSS with S1P supplemented media did not cause a significant change in L_P. Application of S1P-BSA did not cause a significant change in L_P from static to perfused conditions. *, $p < 0.05$, **, $p < 0.01$, ***, $p < 0.001$.

BFF and LSS control conditions at BP and BV respectively (Fig. 7B). Therefore, these findings suggest that the static increase in endothelial permeability in response to S1P is counteracted by associating S1P with albumin.

3.3. Flow-regulated endothelial S1P receptor 1 signaling decreases endothelial permeability

To identify the role of ligand-independent $S1P_1$ activation in modulating endothelial hydraulic conductivity, we monitored changes in L_P after 3-hour pre-treatment with W123, a competitive antagonist of $S1P_1$, followed by exposure to BFF and LSS in the absence of TVF. HUVECs pre-treated with 10 µM W123 and exposed to static conditions over 6 hours did not demonstrate a significant increase in L_P compared to static control conditions (Fig. 8B). In contrast, HUVECs pre-treated with 10 µM W123 and then exposed to BFF and LSS over 6 hours at BP and BV respectively, demonstrated a significant increase in L_P compared to BFF and LSS control conditions at BP and BV (Fig. 8B). The increase in L_P when pre-treated with W123 and exposed to BFF and LSS shows that the decrease in endothelial permeability in response to BFF and LSS is mediated in part by $S1P_1$. These results corroborate previous reports of ligand-independent mechanical activation of $S1P_1$[25,52] and G protein-coupled receptors.[28]

We next monitored changes in endothelial permeability in response to S1P after inhibition of $S1P_1$. HUVECs pre-treated with 10 µM W123 and exposed to 500 nM S1P under static conditions over 6 hours demonstrated a significant decrease in L_P compared to HUVECs exposed to 500 nM S1P under static conditions (Fig. 8B). In contrast, HUVECs pre-treated with 10 µM W123 and then exposed to 500 nM S1P with BFF and LSS over 6 hours at BP and BV respectively, demonstrated a significant increase in L_P compared to HUVECs treated with 500 nM S1P with BFF and LSS conditions at BP and BV (Fig. 8B). Taken together, these results align with previous

reports S1P$_1$ activation decreasing endothelial permeability, particularly under the application of shear stress.[14,53,54]
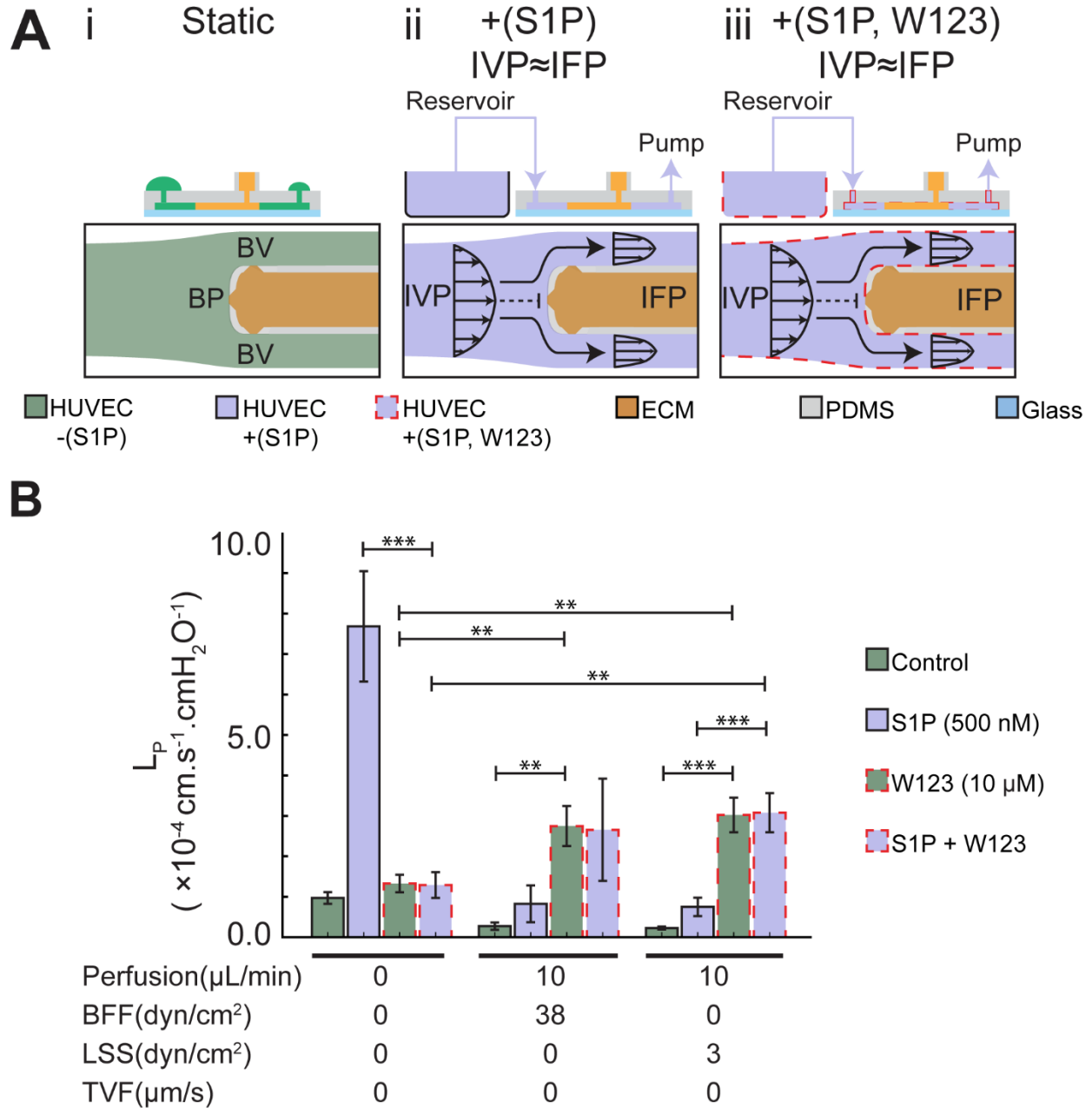
Figure 8. Inhibition of S1P receptor 1 (S1P1) reveals ligand-independent mechanical activation and flow-dependent stabilization in response to S1P. (A) Schematics of the experimental conditions: (i) static control, (ii) perfused microdevice in the absence of transvascular flow (TVF) and addition of S1P (500 nM) in perfusion media, and (iii) perfused microdevice in the absence of TVF and pre-incubation with W123 (10 µM), a competitive antagonist of S1P1 that induces receptor internalization. (B) Quantitative effects of S1P1 inhibition under co-application of S1P with fluid mechanical forces BFF and LSS at the BP and BV respectively. Application of W123 induced ligand-independent increases in L$_P$ under perfused conditions, and increased L$_P$ with the application of S1P under perfusion. **, $p < 0.01$, ***, $p < 0.001$.

3.4. S1P receptor 2 activation elicits flow-regulated response in endothelial permeability

While we anticipated $S1P_1$ activation to stabilize endothelial permeability based on a consensus from previous reports, we next sought to investigate conflicting reports of endothelial response to $S1P_2$ activation, which has demonstrated a tissue-specific response depending on the experimental context. To isolate the endothelial response to $S1P_2$, we monitored changes in L_P after 30 min pre-treatment with JTE-013, a selective antagonist of S1P2, followed by exposure to BFF and LSS in the absence of TVF. HUVECs pre-treated with 200 nM JTE-013 and exposed to static conditions over 6 hours showed no significant change in L_P compared to static control conditions (Fig. 9B). In contrast, HUVECs pre-treated with 200 nM JTE-013 and then exposed to BFF and LSS over 6 hours at BP and BV respectively, demonstrated a significant increase in L_P compared to BFF and LSS control conditions at BP and BV (Fig. 9B). Paralleling the response observed in $S1P_1$, the increase in L_P when pre-treated with JTE-013 and exposed to BFF and LSS demonstrates that the decrease in L_P when subjected to BFF and LSS is mediated in part by $S1P_2$ activation. These results provide new insights into ligand-independent mechanical activation of $S1P_2$ under application of BFF and LSS.

To investigate the role of S1P2 in mediating the HUVEC response to S1P, we pre-treated HUVECs with JTE-013 for 30 min and applied S1P. HUVECs pre-treated with 200 nM JTE-013 and exposed to 500 nM S1P under static conditions over 6 hours demonstrated a significant decrease in L_P compared to HUVECs exposed to 500 nM S1P under static conditions (Fig. 9B). In contrast, HUVECs pre-treated with 200 nM JTE-013 and then exposed to 500 nM S1P with BFF and LSS over 6 hours at BP and BV respectively, demonstrated a significant increase in L_P compared to HUVECs treated with 500 nM S1P with BFF and LSS conditions at BP and BV respectively (Fig. 9B). The differing responses in L_P when pre-treated with JTE-013 and exposed

to 500 nM S1P demonstrates that the endothelial response to S1P$_2$ activation depends on flow

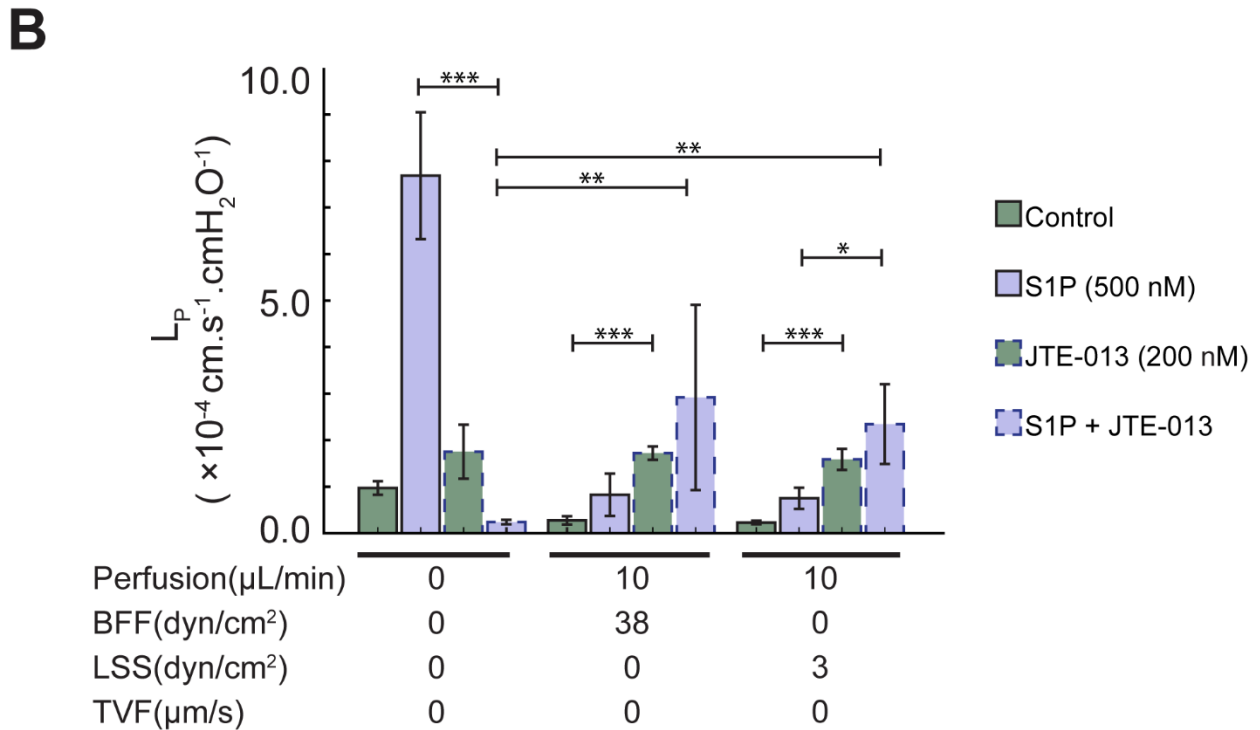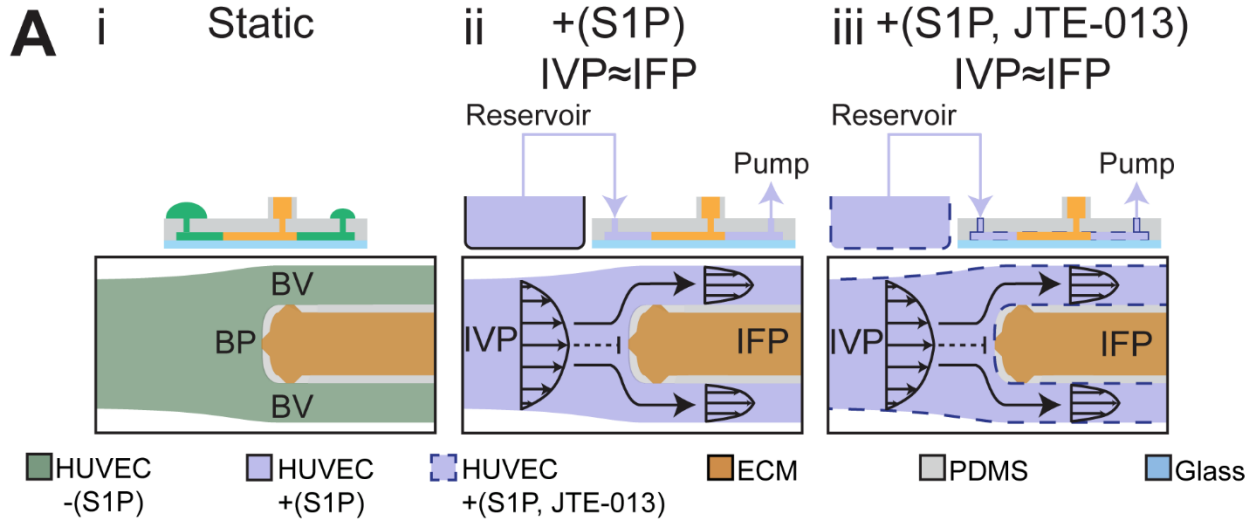
Figure 9. Inhibition of S1P receptor 2 (S1P2) reveals ligand-independent mechanical activation and flow-dependent response to S1P. (A) Schematics of the experimental conditions: (i) static control, (ii) perfused microdevice in the absence of transvascular flow (TVF) and addition of S1P (500 nM) in perfusion media, and (iii) perfused microdevice in the absence of TVF and pre-incubation with JTE-013 (200 nM), a selective antagonist of S1P2. (B) Quantitative effects of S1P2 inhibition under co-application of S1P with fluid mechanical forces BFF and LSS at the BP and BV respectively. Application of JTE-013 induced ligand-independent increases in L$_P$ under perfused conditions, decreased L$_P$ with the application of S1P under static conditions, and increased L$_P$ with the application of S1P under perfused conditions. **, p < 0.01, ***, p < 0.001.

dynamics, showing an increase in endothelial permeability under static conditions and a decrease in endothelial permeability when exposed to BFF and LSS. Taken together, these results may provide further context to the discrepancies in endothelial response to $S1P_2$ activation.

4. SUMMARY AND CONCLUSIONS

Study of endothelial permeability and transendothelial transport is essential to advancing our understanding of the mechanisms that determine vascular development. Current *in vivo* methods enable quantification of vascular permeability with a direct connection to physiology, but these methods often have limited control of the physiochemical microenvironment to isolate the effects of individual mechanisms, particularly mechanical stresses. Microfluidic *in vitro* models present a method to explore the mechanisms governing vascular permeability by enabling precise manipulation of the biomechanical environment experienced by endothelial cells. However, the current state-of-the-art microsystems fail to fully reproduce the complex biophysics that arise due to vessel bifurcations while permitting transendothelial flow and vascular permeability quantification.

This paper reported a microfluidic model that facilitates investigation of flow dynamics generated by vessel bifurcations *in vitro* and enables quantification of endothelial hydraulic conductivity (L_P), which was used to resolve the flow-regulated endothelial response to sphingosine-1-phosphate. We showed that application of bifurcated fluid flow (38 dyn/cm^2 stagnation pressure and approximately zero shear stress) and laminar shear stress (3 dyn/cm^2) at the BP and in each BV, respectively, imparted a time-dependent effect on HUVEC barrier function based on the L_P measurements. (Fig. 6). While L_P increased in response to both BFF and LSS after 1 hour of application, continued perfusion with these forces resulted in stabilization of the HUVEC

25

monolayer after 6 hours, as evidenced by a significant decrease in L_P near the value observed under static treatment after 1 hour and 6 hours of perfusion.

Our findings of the time-dependent effect of LSS on L_P (Fig. 6) are in agreement with previous reports analyzing endothelial permeability using semi-porous transwell assays[55] and templated microfluidic systems housing 3D scaffolds.[56,57] Previously reported measurements in transwell assays[51] suggest that application of LSS causes an initial increase in endothelial permeability that returns to the baseline level during continued application of shear flow. *In vivo* measurements on rabbit carotid arteries[58] and pig coronary venules[59] also demonstrate increased vascular permeability after acute increases in the level of intravascular shear stress, which corroborate the observed effects of LSS *in vitro*.

Furthermore, we established that S1P (500 nM) without albumin chaperones regulated HUVEC barrier function in response to flow dynamics. Application of S1P increased HUVEC L_P under static conditions, but showed no significant effect on L_P under application of BFF and LSS. The flow-dependent response was negated when HUVECs were treated with S1P associated with bovine serum albumin; endothelial permeability was held near static control conditions for S1P-BSA application regardless of static or perfused conditions.

Our conclusions regarding the flow-dependent regulation of endothelial permeability response to S1P signaling are supported by *in vivo* reports of enhanced S1P signaling in the descending mouse aorta when subject to LSS.[14] Previous research established that blood flow can induce $S1P_1$ expression,[10,14,60] which increases barrier function upon S1P activation.[54,61] Furthermore, our conclusions regarding chaperone-dependent signaling of S1P are supported by previous reports of biased-agonism of $S1P_1$ by albumin-bound S1P, and receptor endocytosis in HUVECs.[62] Our results demonstrating the hyperpermeabilization of HUVECs in response to

chaperone-free S1P under static conditions are supported by previous *in vitro* studies that reported pro-angiogenic responses to extravascular application of S1P.[63,64]

A major finding from our study is that BFF and LSS activated both $S1P_1$ and $S1P_2$ signaling to decrease L_P independent of S1P ligand binding (Fig. 8). These results support previous research that suggests ligand-independent shear activation of $S1P_1$ in mouse aortas *in vivo*[14] and HUVECs *in vitro*.[10,14] However, our results also demonstrate ligand-independent activation of $S1P_2$, which provides further support that $S1P_1$ and $S1P_2$ may sense mechanical forces, which has been proposed for other G protein-coupled receptors.[28]

After inhibiting $S1P_1$ with competitive antagonist W123, we demonstrated that application of S1P elicits an increase in endothelial permeability under BFF and LSS. Our observations of the stabilizing effect of $S1P_1$ signaling under flow (Fig. 8) are supported by previous reports $S1P_1$ activation decreasing endothelial permeability when applied with shear stress.[14,53,54] However, our observations of increased permeability after inhibiting $S1P_2$ with selective antagonist JTE-013 and applying S1P with BFF and LSS demonstrate a stabilizing effect of $S1P_2$ that diverges from previous reports. Previous literature supports a role for $S1P_2$ in vascular barrier disruption during anaphylaxis in mice[65] and pathological angiogenesis,[66] but previous studies have also established an anti-angiogenic role for $S1P_2$ within tumor vasculature.[22] These results indicate tissue-dependent responses, any may also be influenced by the fluid mechanical environment. The discrepancy between the consensus regarding the role of $S1P_1$ and conflicting reports regarding the role of $S1P_2$ may stem from differences in G protein-coupling; while $S1P_1$ couples exclusively with Gαi/o, $S1P_2$ can couple with Gαi/o, Gαq, and Gα12/13.[10] Further exploration of $S1P_1$- and $S1P_2$-induced G protein activation in endothelial cells from different tissue origins and under

different flow dynamics may provide further insights into the mechanisms leading to conflicting roles of $S1P_2$.

In this report, we have demonstrated the first observation of the stabilizing effect of bifurcated fluid flow, to our knowledge. Furthermore, we have applied the strengths of our microfluidic model of a vessel bifurcation to report the ligand-independent mechanical activation of sphingosine-1-phosphate receptors 1 and 2, providing further support for the role of G protein-coupled receptors as mechanosensors. Taken together, our results provide further insights into how flow dynamics integrate with biochemical signals to direct vascular development. Further studies of the mechanotransduction pathways of LSS and BFF within ECs, which are uniquely enabled by our novel microfluidic model, will provide insights into the mechanisms responsible for converting these mechanical stresses into biological responses.

References

1.	Carmeliet, P. & Jain, R. K. Molecular mechanisms and clinical applications of angiogenesis. *Nature* **473,** 298–307 (2011).
2.	Curry, F.-R. E. Permeability measurements in an individually perfused capillary: the 'squid axon' of the microcirculation (1974). *Exp. Physiol.* **93,** 444–6 (2008).
3.	Curry, F. R. E. Microvascular solute and water transport. *Microcirculation* **12,** 17–31 (2005).
4.	Di Lorenzo, A. *et al.* eNOS-derived nitric oxide regulates endothelial barrier function through VE-cadherin and Rho GTPases. *J. Cell Sci.* **127,** 2120–2120 (2014).
5.	Chrobak, K. M., Potter, D. R. & Tien, J. Formation of perfused, functional microvascular tubes in vitro. *Microvasc. Res.* **71,** 185–196 (2006).
6.	Tarbell, J. M. Mass Transport in Arteries and the Localization of Atherosclerosis. *Annu. Rev. Biomed. Eng.* **5,** 79–118 (2003).
7.	Claesson-Welsh, L. & Welsh, M. VEGFA and tumour angiogenesis. *J. Intern. Med.* **273,** 114–127 (2013).
8.	Hla, T., Venkataraman, K. & Michaud, J. The vascular S1P gradient-Cellular sources and biological significance. *Biochim. Biophys. Acta - Mol. Cell Biol. Lipids* **1781,** 477–482 (2008).
9.	Venkataraman, K. *et al.* Vascular endothelium as a contributor of plasma sphingosine 1-phosphate. *Circ. Res.* **102,** 669–676 (2008).
10.	Yanagida, K. & Hla, T. Vascular and Immunobiology of the Circulatory Sphingosine 1-Phosphate Gradient. *Annu. Rev. Physiol.* **79,** 67–91 (2017).
11.	Akbari, E., Spychalski, G. B. & Song, J. W. Microfluidic approaches to the study of angiogenesis and the microcirculation. *Microcirculation* **24,** 1–8 (2017).
12.	Ikeda, M., Kihara, A. & Igarashi, Y. Sphingosine-1-phosphate lyase SPL is an endoplasmic reticulum-resident, integral membrane protein with the pyridoxal 5′-phosphate binding domain exposed to the cytosol. *Biochem. Biophys. Res. Commun.* **325,** 338–343 (2004).
13.	Wilkerson, B. A., Grass, G. D., Wing, S. B., Argraves, W. S. & Argraves, K. M. Sphingosine 1-phosphate (S1P) carrier-dependent regulation of endothelial barrier: High density lipoprotein (HDL)-S1P prolongs endothelial barrier enhancement as compared with albumin-S1P via effects on levels, trafficking, and signaling of S1P1. *J. Biol. Chem.* **287,** 44645–44653 (2012).
14.	Jung, B. *et al.* Flow-Regulated Endothelial S1P Receptor-1 Signaling Sustains Vascular Development. *Dev. Cell* **23,** 600–610 (2012).
15.	Gaengel, K. *et al.* The Sphingosine-1-Phosphate Receptor S1PR1 Restricts Sprouting Angiogenesis by Regulating the Interplay between VE-Cadherin and VEGFR2. *Dev. Cell* **23,** 587–599 (2012).
16.	Paik, J. H. *et al.* Sphingosine 1-phosphate receptor regulation of N-cadherin mediates vascular stabilization. *Genes Dev.* **18,** 2392–2403 (2004).
17.	Igarashi, J. & Michel, T. Sphingosine-1-phosphate and modulation of vascular tone. *Cardiovasc. Res.* **82,** 212–220 (2009).
18.	Wang, L. & Dudek, S. M. Regulation of vascular permeability by sphingosine 1-phosphate. *Microvasc. Res.* **77,** 39–45 (2009).
19.	Xiong, Y. & Hla, T. in *Current Topics in Microbiology and Immunology* **378,** 85–105

(2014).

20.   Blaho, V. A. & Hla, T. An update on the biology of sphingosine 1-phosphate receptors. *J. Lipid Res.* **55,** 1596–1608 (2014).

21.   Kono, M. *et al.* The sphingosine-1-phosphate receptors S1P1, S1P2, and S1P3 function coordinately during embryonic angiogenesis. *J. Biol. Chem.* **279,** 29367–29373 (2004).

22.   Du, W. *et al.* S1P2, the G protein-coupled receptor for sphingosine-1- phosphate, negatively regulates tumor angiogenesis and tumor growth in vivo in mice. *Cancer Res.* **70,** 772–781 (2010).

23.   Morales-Ruiz, M. *et al.* Sphingosine 1-Phosphate Activates Akt, Nitric Oxide Production, and Chemotaxis through a Gi Protein/Phosphoinositide 3-Kinase Pathway in Endothelial Cells. *J. Biol. Chem.* **276,** 19672–19677 (2001).

24.   Hughes, S. K., Wacker, B. K., Kaneda, M. M. & Elbert, D. L. Fluid shear stress modulates cell migration induced by sphingosine 1-phosphate and vascular endothelial growth factor. *Ann. Biomed. Eng.* **33,** 1003–1014 (2005).

25.   Aoki, S., Osada, M., Kaneko, M., Ozaki, Y. & Yatomi, Y. Fluid shear stress enhances the sphingosine 1-phosphate responses in cell-cell interactions between platelets and endothelial cells. *Biochem. Biophys. Res. Commun.* **358,** 1054–1057 (2007).

26.   Curry, F. E. & Adamson, R. H. Endothelial glycocalyx: Permeability barrier and mechanosensor. *Ann. Biomed. Eng.* **40,** 828–839 (2012).

27.   Shyy, J. Y. J. & Chien, S. Role of integrins in endothelial mechanosensing of shear stress. *Circ. Res.* **91,** 769–775 (2002).

28.   Chachisvilis, M., Zhang, Y.-L. & Frangos, J. A. G protein-coupled receptors sense fluid shear stress in endothelial cells. *Proc. Natl. Acad. Sci.* **103,** 15463–15468 (2006).

29.   Ghaffari, S., Leask, R. L. & Jones, E. A. V. Simultaneous imaging of blood flow dynamics and vascular remodelling during development. *Development* 4158–4167 (2015). doi:10.1242/dev.127019

30.   Ghaffari, S., Leask, R. L. & Jones, E. A. V. Blood flow can signal during angiogenesis not only through mechanotransduction, but also by affecting growth factor distribution. *Angiogenesis* **20,** 373–384 (2017).

31.   Galie, P. A. *et al.* Fluid shear stress threshold regulates angiogenic sprouting. *Proc. Natl. Acad. Sci.* **111,** 7968–7973 (2014).

32.   Song, J. W. & Munn, L. L. Fluid forces control endothelial sprouting. *Proc. Natl. Acad. Sci. U. S. A.* **108,** 15342–15347 (2011).

33.   Song, J. W., Daubriac, J., Tse, J. M., Bazou, D. & Munn, L. L. RhoA mediates flow-induced endothelial sprouting in a 3-D tissue analogue of angiogenesis. *Lab Chip* **12,** 5000 (2012).

34.   Fu, B. M. & Shen, S. Acute VEGF effect on solute permeability of mammalian microvessels in vivo. *Microvasc. Res.* **68,** 51–62 (2004).

35.   Miles, A. A. & Miles, E. M. Vascular reactions to histamine, histamine-liberator and leukotaxine in the skin of guinea-pigs. *J. Physiol.* **118,** 228–257 (1952).

36.   Bogorad, M. I. *et al.* In vitro microvessel models. *Lab Chip* **15,** 4242–4255 (2015).

37.   Morgan, J. P. *et al.* Formation of microvascular networks in vitro. *Nat. Protoc.* **8,** 1820–1836 (2013).

38.   Bogorad, M. I., DeStefano, J., Wong, A. D. & Searson, P. C. Tissue-engineered 3D microvessel and capillary network models for the study of vascular phenomena. *Microcirculation* **24,** 1–12 (2017).

39. Van Duinen, V. *et al.* 96 Perfusable Blood Vessels To Study Vascular Permeability in Vitro. *Sci. Rep.* **7,** 1–11 (2017).

40. Wong, K. H. K., Chan, J. M., Kamm, R. D. & Tien, J. Microfluidic Models of Vascular Functions. *Annu. Rev. Biomed. Eng.* **14,** 205–230 (2012).

41. Tien, J. Microfluidic approaches for engineering vasculature. *Curr. Opin. Chem. Eng.* **3,** 36–41 (2014).

42. Akbari, E., Spychalski, G. B., Rangharajan, K. K., Prakash, S. & Song, J. W. Flow dynamics control endothelial permeability in a microfluidic vessel bifurcation model. *Lab Chip* 1084–1093 (2018). doi:10.1039/C8LC00130H

43. Bischel, L. L., Beebe, D. J. & Sung, K. E. Microfluidic model of ductal carcinoma in situ with 3D, organotypic structure. *BMC Cancer* **15,** 1–10 (2015).

44. Davis, G. E., Bayless, K. J. & Mavila, A. Molecular basis of endothelial cell morphogenesis in three-dimensional extracellular matrices. *Anat. Rec.* **268,** 252–275 (2002).

45. Gooch, K., Dangler, C. & Frangos, J. Exogenous, basal, and flow-induced nitric oxide production and endothelial cell proliferation. *J Cell Physiol* **171,** 252–258 (1997).

46. Starling, E. H. On the absorption of fluids from the connective tissue spaces. *J Physiol* **19,** 265–273 (1896).

47. Turner, M. R. Effects of proteins on the permeability of monolayers of cultured bovine arterial endothelium. *J. Physiol.* **449,** 21–35 (1992).

48. Hammer, A. M. *et al.* Stromal PDGFR-α Activation Enhances Matrix Stiffness, Impedes Mammary Ductal Development, and Accelerates Tumor Growth. *Neoplasia (United States)* **19,** 496–508 (2017).

49. Swartz, M. A. & Fleury, M. E. Interstitial Flow and Its Effects in Soft Tissues. *Annu. Rev. Biomed. Eng.* **9,** 229–256 (2007).

50. Tarbell, J. M. Shear stress and the endothelial transport barrier. *Cardiovasc. Res.* **87,** 320–330 (2010).

51. Pang, Z., Antonetti, D. A. & Tarbell, J. M. Shear stress regulates HUVEC hydraulic conductivity by occludin phosphorylation. *Ann. Biomed. Eng.* **33,** 1536–1545 (2005).

52. Givens, C. & Tzima, E. S1P1 Bridges Mechanotransduction and Angiogenesis during Vascular Development. *Dev. Cell* **23,** 451–452 (2012).

53. Oo, M. L. *et al.* Engagement of S1P 1 -degradative mechanisms leads to vascular leak in mice Find the latest version : Engagement of S1P 1 -degradative mechanisms leads to vascular leak in mice. **121,** 2290–2300 (2011).

54. Christensen, P. M. *et al.* Impaired endothelial barrier function in apolipoprotein M-deficient mice is dependent on sphingosine-1-phosphate receptor 1. *FASEB J.* **30,** 2351–2359 (2016).

55. Colgan, O. C. *et al.* Regulation of bovine brain microvascular endothelial tight junction assembly and barrier function by laminar shear stress. *Am. J. Physiol. Heart Circ. Physiol.* **292,** 3190–3197 (2007).

56. Price, G. M. *et al.* Effect of mechanical factors on the function of engineered human blood microvessels in microfluidic collagen gels. *Biomaterials* **31,** 6182–6189 (2010).

57. Buchanan, C. F., Verbridge, S. S., Vlachos, P. P. & Rylander, M. N. Flow shear stress regulates endothelial barrier function and expression of angiogenic factors in a 3D microfluidic tumor vascular model. *Cell Adh. Migr.* **8,** 517–524 (2014).

58. Lever, M., Tarbell, J. & Caro, C. The effect of luminal flow in rabbit carotid artery on

transmural fluid transport. *Exp. Physiol.* **77,** 553–563 (1992).

59. Yuan, Y., Granger, H. J., Zawieja, D. C. & Chilian, W. M. Flow modulates coronary venular permeability by a nitric oxide-related mechanism. *Am. J. Physiol.* **263,** H641-6 (1992).

60. Takada, Y., Kato, C., Kondo, S., Korenaga, R. & Ando, J. Cloning of cDNAs encoding G protein-coupled receptor expressed in human endothelial cells exposed to fluid shear stress. *Biochem. Biophys. Res. Commun.* **240,** 737–741 (1997).

61. Oo, M. L. *et al.* Engagement of S1P 1 -degradative mechanisms leads to vascular leak in mice. *J Clin Invest* **121,** 2290–2300 (2011).

62. Galvani, S. *et al.* HDL-bound sphingosine 1-phosphate acts as a biased agonist for the endothelial cell receptor S1P1 to limit vascular inflammation. *Sci. Signal.* **8,** 1–10 (2015).

63. Nguyen, D.-H. T. *et al.* Biomimetic model to reconstitute angiogenic sprouting morphogenesis in vitro. *Proc. Natl. Acad. Sci.* **110,** 6712–6717 (2013).

64. Bayless, K. J. & Davis, G. E. Sphingosine-1-phosphate markedly induces matrix metalloproteinase and integrin-dependent human endothelial cell invasion and lumen formation in three-dimensional collagen and fibrin matrices. *Biochem. Biophys. Res. Commun.* **312,** 903–913 (2003).

65. Olivera, A. *et al.* Sphingosine kinase 1 and sphingosine-1- phosphate receptor 2 are vital to recovery from anaphylactic shock in mice. **120,** (2010).

66. Skoura, A. *et al.* Essential role of sphingosine 1 – phosphate receptor 2 in pathological angiogenesis of the mouse retina. *J. Clin. Invest.* **117,** 2506–16 (2007).